Analysis and modeling of hydrothermal plume data acquired from the 85°E segment of the Gakkel Ridge

Christian Stranne,[1] Robert A. Sohn,[2] Bengt Liljebladh,[1] and Ko-ichi Nakamura[3]

Received 2 September 2009; revised 23 December 2009; accepted 12 January 2010; published 30 June 2010.

[1] We use data from a CTD plume-mapping campaign conducted during the Arctic Gakkel Vents (AGAVE) expedition in 2007 to constrain the nature of hydrothermal processes on the Gakkel Ridge at 85°E. Thermal and redox potential (*Eh*) anomalies were detected in two discrete depth intervals: 2400–2800 m (Interval 1) and 3000–3800 m (Interval 2). The spatial and temporal patterns of the signals indicate that the Interval 1 anomalies were most likely generated by a single large, high-temperature (T > 100°C) vent field located on the fault terraces that form the NE axial valley wall. In contrast, the Interval 2 anomalies appear to have been generated by up to 7 spatially distinct vent fields associated with constructional volcanic features on the floor of the axial valley, many of which may be sites of diffuse, low-temperature (T < 10°C) discharge. Numerical simulations of turbulent plumes rising in a weakly stratified Arctic Ocean water column indicate that the high-temperature field on the axial valley wall has a thermal power of ~1.8 GW, similar to the Trans-Atlantic Geotraverse and Rainbow fields in the Atlantic Ocean, whereas the sites on the axial valley floor have values ranging from 5 to 110 MW.

Citation: Stranne, C., R. A. Sohn, B. Liljebladh, and K. Nakamura (2010), Analysis and modeling of hydrothermal plume data acquired from the 85°E segment of the Gakkel Ridge, *J. Geophys. Res.*, *115*, C06028, doi:10.1029/2009JC005776.

1. Introduction

[2] The ultraslow-spreading Gakkel Ridge, which stretches for ~1800 km across the eastern Arctic Basin [e.g., *Sella et al.*, 2002], has represented something of an enigma for hydrothermal research since the Arctic Mid-Ocean Ridge Expedition (AMORE) found evidence for water column anomalies in over 80% of 145 Miniature-Autonomous-Plume-Recorder (MAPR) casts along ~850 km of the ridge in 2001 [*Edmonds et al.*, 2003]. This high frequency of plume observations is starkly at odds with well-established trends for the global mid-ocean ridge (MOR) system based on spreading rate [*Michael et al.*, 2003], which are believed to reflect the first-order relationship between heat flux and the divergence rate across spreading plate boundaries [*Baker et al.*, 1996].

[3] There are at least two possible reasons why hydrothermal plume fluids were so commonly observed along the Gakkel Ridge during the AMORE field program in 2001. The geological nature of crustal accretion and extension at ultraslow-spreading MORs (located predominantly in the Indian and Arctic Oceans) is significantly different than faster spreading MORs in the rest of the ocean basins [e.g., *Dick et al.*, 2003], and these mechanical and compositional differences may increase the total amount of heat available to drive hydrothermal convection per unit distance along the spreading axis [e.g., *German and Lin*, 2004]. For example, increased penetration depth of faults hosting fluid flow [e.g., *deMartin et al.*, 2007] may thicken the layer in which hydrothermal heat is extracted. Alternatively, the Gakkel Ridge represents a deep, topographic channel that may trap hydrothermal plumes and limit their interaction with the rest of the Arctic Ocean, thereby allowing them to be detected at great distance along the ridge axis from their source regions [e.g., *Edmonds et al.*, 2003; *Michael et al.*, 2003].

[4] *Baker et al.* [2004] conducted a detailed analysis of MAPR cross sections from AMORE and concluded that the large number of plume anomalies observed along the Gakkel Ridge were generated by as few as eight vent fields, supporting the hypothesis that plume fluids were detected at long distances from their seafloor source regions. *Baker et al.* [2004] further hypothesized that hydrothermal fluids from a very large source located on the 85°E segment in the Eastern Volcanic Zone were detected at distances of up to 175 km along the ridge axis. The 85°E site is of particular interest because it generated a large earthquake swarm in 1999, which has been associated with volcanic activity [e.g., *Edwards et al.*, 2001; *Mueller and Jokat*, 2000; *Sohn et al.*, 2008; *Tolstoy et al.*, 2001], and there is seismic evidence that this eruption was ongoing during the AMORE surveys in 2001 [*Schlindwein et al.*, 2007]. Unfortunately, the water column plume data acquired from the 85°E site during AMORE is limited to MAPR profiles from seven rock dredges/cores, and a single CTD hydrocast, all of which

[1]Department of Earth Sciences, University of Gothenburg, Gothenburg, Sweden.
[2]Woods Hole Oceanographic Institution, Woods Hole, Massachusetts, USA.
[3]National Institute of Advanced Industrial Science and Technology, Tsukuba, Japan.

0148-0227/10/2009JC005776

were conducted within a relatively small region near the center of the axial valley [*Edmonds et al.*, 2003]. These data provide intriguing evidence for a potentially large hydrothermal field, but they are too limited to constrain the nature of hydrothermal venting at the 85°E site, and its relationship to recent volcanic activity.

[5] In this paper we present results from a more comprehensive CTD plume-mapping campaign on the 85°E segment of the Gakkel Ridge conducted during the Arctic Gakkel Vents (AGAVE) expedition in 2007, and we use these data in concert with numerical simulations of hydrothermal plumes rising in a weakly stratified Arctic Ocean to place new constraints on the number and heat flux of discrete seafloor vent fields. Our results provide evidence for up to eight distinct seafloor discharge sites, one of which appears to be a large, high-temperature (T > 100°C) field located on the fault terrace forming the northern axial valley wall, and the rest of which appear to be much smaller, perhaps low-temperature (T < 10°C) fields associated with constructional volcanic features on the axial valley floor.

2. Site Description

2.1. Oceanography of the 85°E Site

[6] The Gakkel Ridge divides the Eurasian Basin into two subbasins; the Nansen and the Amundsen Basins with maximum depths of ~4000 m and ~4500 m, respectively. Basin waters below ~2500 m are isolated from surrounding oceans. The estimated isolation age, based on C^{14} measurements is ~250 years for the Nansen Basin and somewhat less for the Amundsen Basin [*Schlosser et al.*, 1997]. Hydrographic data show that the deep water of the basins are remarkably homogeneous but somewhat different, the Amundsen Basin being both colder and more saline [*Jones et al.*, 1995] than the Nansen Basin. *Björk and Winsor* [2006] noted that the homogeneous bottom layers observed in the Nansen and Amundsen basins were absent from CTD profiles acquired over the Gakkel ridge.

[7] There are very few measurements to constrain bottom current velocities on the Gakkel Ridge. Hydrographic and tracer data have been interpreted to indicate that the circulation in the Arctic Ocean, both in the upper and lower layers, follows topography with a rather weak westward drift along the Gakkel ridge [*Jones et al.* 1995]. This is consistent with bottom current estimates derived from an AUV survey during the AGAVE expedition, which averaged to 1 cm/s westward along the axial valley over one diurnal tidal cycle. Models of the geostrophic bottom velocities [*Nøst and Isachsen*, 2003] indicate a more complex circulation with a cyclonic gyre in both basins, implying a weak easterly flow on the Amundsen Basin side and a weak westward flux on the Nansen Basin side of the Gakkel Ridge. The topography of the Gakkel Ridge is rough on scales not properly resolved in such models, however. The horizontal velocities due to the barotropic tide are weak at the eastern part of the ridge being, for the time of the cruise, in the range 0 – 1.25 cm/s for the 85°E site [*Padman and Erofeeva*, 2004].

2.2. Geology of the 85°E Site

[8] The axial valley of the Gakkel Ridge at 85°E consists of a ~15 km wide by ~1 km deep axial valley containing several ridge-parallel constructional volcanic lineations. All but one of our CTD surveys was conducted within a 7 × 11 km region centered over the volcanic features at ~85°37′N, ~85°15′E (Figure 1), which corresponds to the location of the strongest plume anomalies observed in 2001. A single survey was conducted outside this zone traversing the northern wall of the axial valley at an oblique angle (Figure 1).

[9] A set of 7 MAPR casts and 1 CTD cast were previously acquired from this site during the AMORE expedition in 2001, producing the largest hydrothermal plume anomalies detected over ~850 km of the Gakkel Ridge during that field program [*Edmonds et al.*, 2003]. There are at least two distinct plume horizons in the 2001 data, implying the existence of multiple seafloor discharge sites. The largest plume anomaly (maximum $\delta\Theta$ of 0.07°C) was up to 1400 m thick and was centered at a depth of ~2500 m. A smaller plume anomaly, ~200 m thick, was observed at a depth of ~3300 m. The large plume anomaly resides more than 1 km above the local seafloor, suggesting a rise height more than twice as high as any other known hydrothermal plume on the global mid-ocean ridge system [e.g., *Speer and Rona*, 1989]. The size and apparent rise height of the plume have been taken as evidence of a massive source field (~3.6 GW) that generated detectable anomalies as far as 175 km to the west along the rise axis [*Baker et al.*, 2004].

[10] Seismic data from the Global Seismic Network (GSN) [*Mueller and Jokat*, 2000; *Tolstoy et al.*, 2001] and acoustic backscatter data acquired during the SCICEX expedition [*Edwards et al.*, 2001] have been interpreted to indicate that the 85°E site experienced a large volcanic eruption in 1999, but seafloor camera surveys during the AGAVE expedition in 2007 revealed only a few small lava flows fresh enough to have erupted within the past decade [*Willis et al.*, 2007]. However, the seafloor throughout the entire axial valley is blanketed with volcaniclastic material that appears to have been generated by explosive submarine eruptions [*Sohn et al.*, 2008], and explosive reports originating from the seafloor at this site were detected by a local network of ice-mounted seismometers in 2001 [*Schlindwein et al.*, 2007]. The chemistry of plume fluids acquired during the AGAVE expedition indicate that the large, upper level plume is not an "event" plume from a volcanic eruption in 1999 [*Upchurch et al.*, 2007], but the water column signature of deep sea explosive volcanic eruptions is not known. Although it seems likely that recent volcanic activity has stimulated hydrothermal discharge in this region, the relationship between volcanic activity, hydrothermal activity, and the water column plume anomalies observed at the 85°E site is not clear.

3. Instruments and Methods

[11] In this paper we consider two types of plume data; thermal anomalies based on the deviation of potential temperature from the background profile ($\delta\Theta$), and chemical anomalies based on the fluid redox potential (*Eh*). We selected a CTD profile without any detectable plume anomalies and filtered it with a fifth-order, low-pass Butterworth filter (cutoff frequency of 1/50 s^{-1}) to generate a nominal "background" field. Thermal anomalies were then defined as the deviation in potential temperature, Θ, with reference pressure at 3000 dbar, from the background profile (Figure 2). The strength of an *Eh* anomaly is related to the

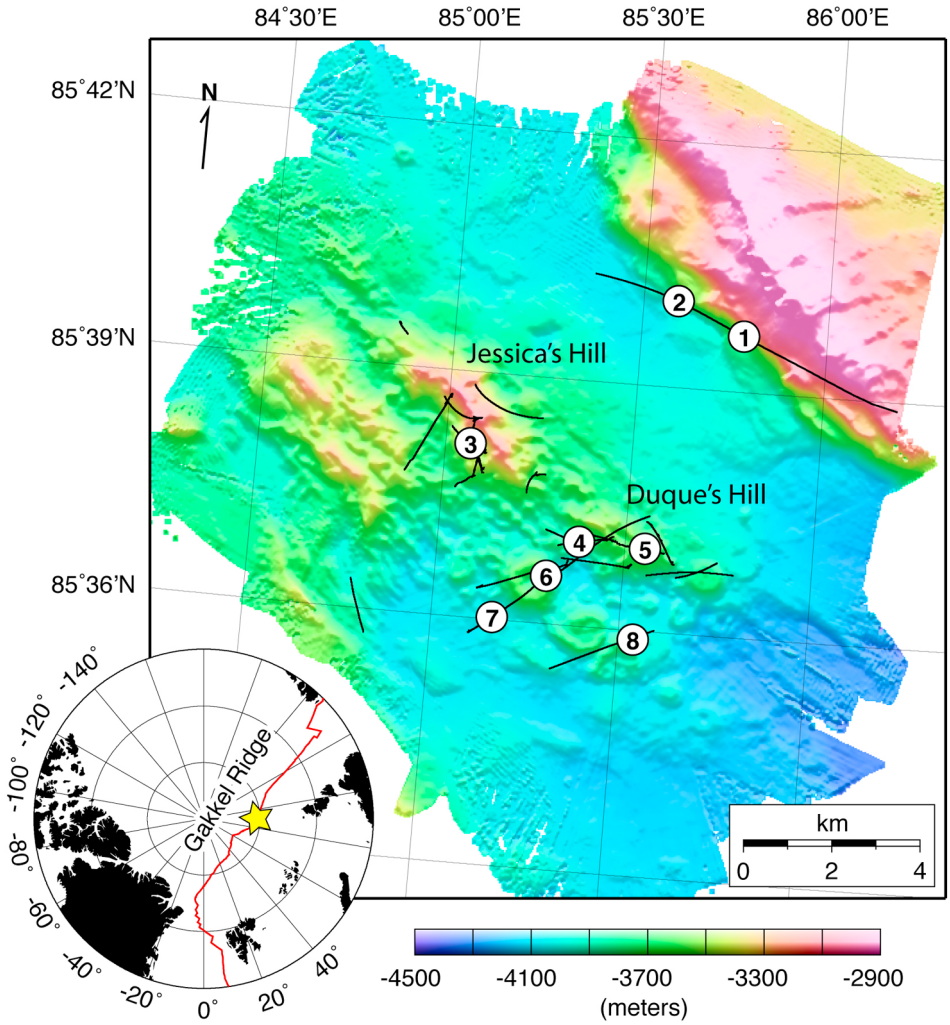

Figure 1. Bathymetry of the 85°E segment of the Gakkel Ridge with location within the Arctic Basin shown in inset. CTD track lines during the AGAVE expedition in 2007 shown as black lines. Location of the maximum temperature anomalies associated with each inferred discrete seafloor discharge site (Table 4) shown as white numbered circles.

time rate of change, rather than absolute magnitude, of the *Eh* measurement. Therefore we define the *Eh* anomaly as the maximum (negative) value of the time derivative (*Eh'*) in a given depth interval. We use the thermal and chemical anomalies together to constrain the distribution of hydrothermal sources on the seafloor.

[12] The CTD data were acquired with a Sea-Bird SBE 9+ pumped system with dual conductivity (SBE 4Cs) and dual temperature (SBE 3+) sensors. Accuracy of the temperature and conductivity sensors was nominally 0.001°C and 0.003 S/m, respectively. The CTD rosette package was outfitted with 22 10 L Niskin bottles, which were used to acquire samples for chemical analyses [*Upchurch et al.*, 2007]. The CTD rosette was raised and lowered through the water column (typically between 2500 m depth to just above the local seafloor) while the icebreaker drifted passively with the ice. We only analyze data from CTD "downcasts" (i.e., when the CTD is being lowered through the water column) because measurements acquired during "upcasts" are influenced by the wake of the CTD rosette frame and sensor package. Because the ship cannot maneuver during the CTD surveys, but rather must passively drift with the ice, it is not possible to acquire linear, well-aligned water column transects. Therefore, considerable effort was made to monitor and forecast the ice drift so as to acquire data within regions of specific interest. Drift speeds varied between 0 and 0.2 m/s with typical values of ~0.1 m/s, and the drift direction varied typically within a few hours in response to changes in wind speed/direction and inertial oscillations. These effects complicated the ice drift predictions considerably. Overall, the CTD data were acquired at very slow speeds and in directions that were not optimal for the hydrothermal plume surveys we were attempting to conduct, which fundamentally limited the efficiency and efficacy of our surveys.

[13] *Eh* was measured as the voltage difference between a Pt electrode and a reference electrode through the SBE 9+ auxiliary channel. The Pt electrode was a 0.7 mm diameter pure Pt wire without any polishing mechanism. The Pt electrode was refreshed several times during the CTD surveys by immersion in a diluted HCl solution. The reference

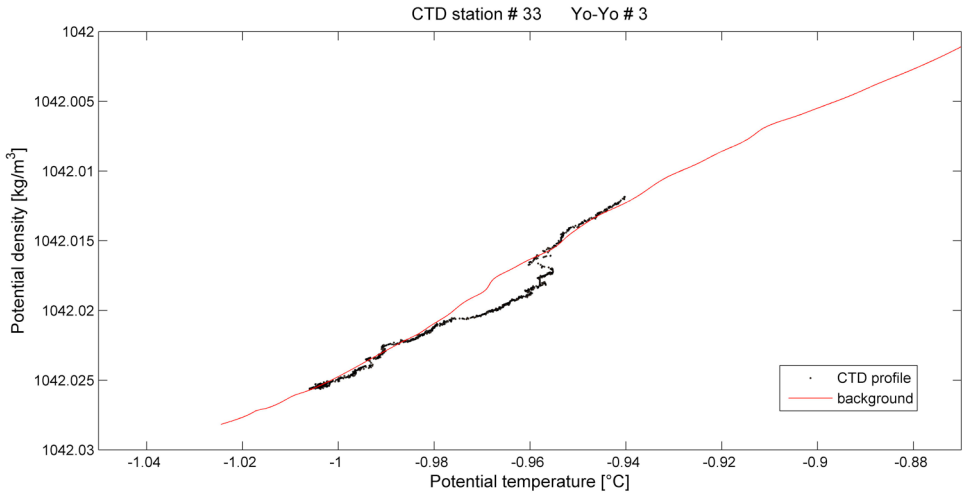

Figure 2. An example of a CTD profile with a temperature anomaly compared to the background density profile. The potential density range of the anomaly corresponds to a depth range of approximately 3400–3800 m (taken from a down cast close to source 6, Figure 1).

electrode was a Ag-AgCl electrode sealed in a saturated KCl solution with a porous ceramic plug as an electric junction. A transformer was inserted between the electrodes and the CTD to separate the electric ground and transmit the voltage in an acceptable range for the SBE 9+ auxiliary channel. The *Eh* value used in this paper analysis was the raw Pt electrode voltage value against Ag-AgCl reference electrode in saturated KCl solution, and not the *Eh* values against a hydrogen standard electrode as is standard in electrochemistry.

[14] We estimated the latitude and longitude of the CTD on the basis of the ship's GPS data (corrected for offset between GPS antennae and CTD deployment site on the bow), and note the corresponding measurement depth. We then estimate the seafloor depth immediately below the measurement on the basis of bathymetric data acquired during the AGAVE expedition, gridded at 30 m X-Y intervals. We assumed that the wire angle was vertical for the CTD position estimate because the ice drift velocities were very slow (~0.2 kt).

4. Plume Observations

[15] Hydrothermal plumes rise vertically and then spread laterally once enough ambient seawater has been entrained to obtain neutral density of the mixture with respect to the stratified water column [*Turner*, 1986]. To first order, the rise height of a plume is controlled by the thermal power (i.e., heat flux) of the source vent [*Turner*, 1973], such that the presence of multiple plume anomaly depth horizons implies the existence of multiple seafloor sources. In addition, the horizontal distribution of thermal and chemical anomalies detected within a similar depth horizon can also be used to detect multiple sources. We can therefore use the vertical and horizontal distribution of the plume anomalies to constrain the number and heat flux of seafloor source vents.

[16] Hydrothermal plume anomalies were detected within two distinct depth bands during the AGAVE expedition; a shallow horizon corresponding to depths of 2400–2800 m with thermal anomalies of 0.008 – 0.021°C (Interval 1), and a deeper horizon corresponding to depths of 3000–3800 m (Interval 2) with thermal anomalies of 0 – 0.015°C (only potential temperature anomalies larger than 0.003 are considered). These same plume horizons were observed during the AMORE expedition, but the magnitude of the thermal anomalies in Interval 1 were considerably larger in 2001 (max values of up to 0.07°C) [*Edmonds et al.*, 2003], which has important implications for plume source mechanisms (see Discussion).

4.1. Interval 1 (2400–2800 m)

[17] Thermal anomalies in this "upper" depth interval were detected intermittently during various CTD casts over constructional volcanic features within the axial valley, but were strongest with $\delta\Theta > 0.02$°C on a section that obliquely traversed the northern wall of the axial valley (Figure 3). The anomalies detected within the axial valley were generally smaller ($\delta\Theta < 0.01$°C) - although a single anomaly of 0.015°C was found just south of Duque's Hill. None of the thermal anomalies in this depth interval were associated with corresponding *Eh* anomalies.

[18] Based on our data we find evidence for one or two discrete seafloor sources contributing to the anomalies observed in this depth interval. There may be just a single source located near the northern axial valley wall, but there could also conceivably be a second source within the axial valley. We prefer to interpret the anomalies as having been generated by a single source on the axial valley wall because the rise height to Interval 1 for a vent field on the axial valley floor is > 1000 m, which would require an extremely large and powerful source, and it seems highly unlikely that such a source would generate the kind of patchy, intermittent, anomalies that we observed in this interval over the axial valley. Instead, these intermittent anomalies are more likely explained by spatial aliasing associated with topographically controlled advection and possibly also eddy formation [*Thorpe*, 2005]. The data are therefore most consistent with a single source from a site elevated above the axial valley floor on the fault terrace that generates the NE valley wall (Figure 4). The lack of *Eh* anomalies in Interval 1 indicates that the fluid were not "fresh," but rather

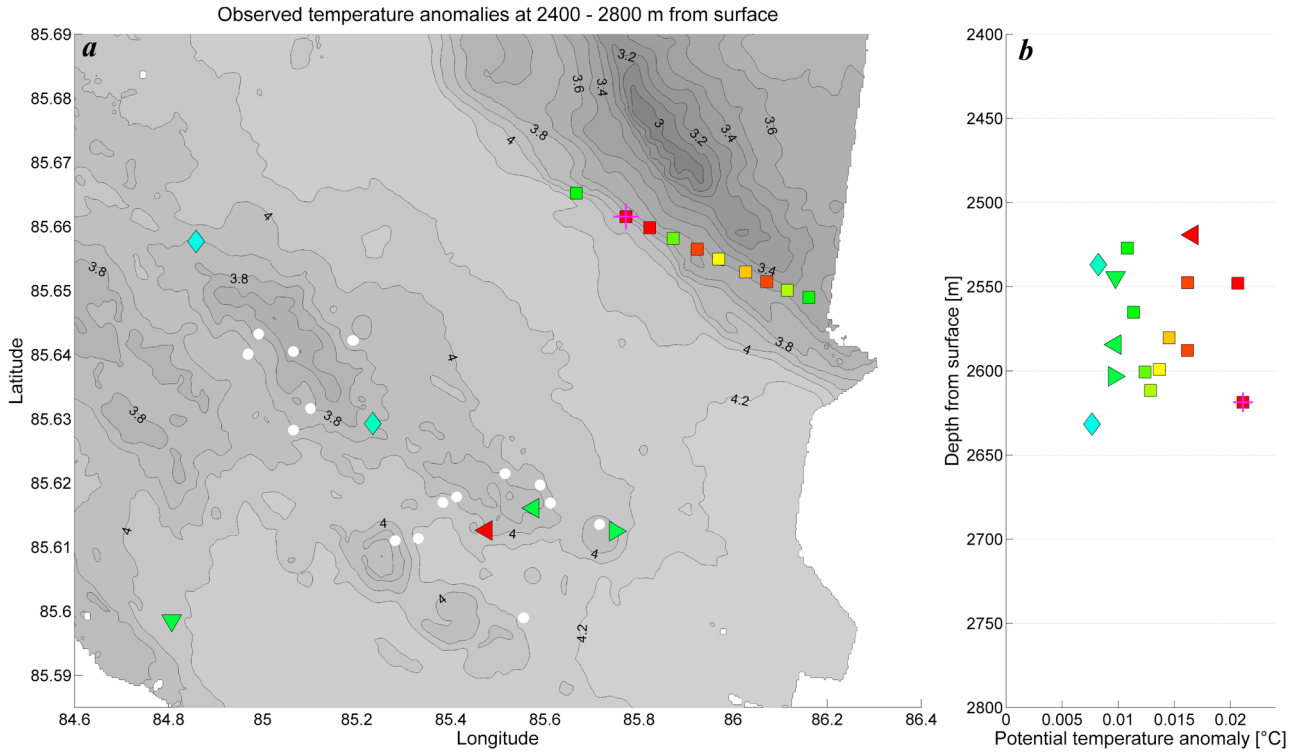

Figure 3. The (a) horizontal and (b) vertical distributions of the observed temperature anomalies in depth Interval 1 (2400–2800 m). White circles indicate "blanks," i.e., CTD profiles where no anomalies were detected. The magenta cross indicates the maximum anomaly detected in this depth interval. The gray contours indicate bottom depth in km.

had been in the water column long enough to lose their initial redox potential. The timescale for redox equilibration of plume fluids is not well constrained, particularly in the Arctic Ocean, but *Eh* anomalies due to Fe(II) are expected to equilibrate within a day, regardless of ocean basin. This uncertainty, combined with the slow bottom current speeds in this area (~1 cm/s), make it difficult to interpret the lack of *Eh* anomalies in Interval 1, but it is probably safe to say that none of our surveys passed directly above the source generating the plume signals we observed in this depth interval.

[19] We use the depth and magnitude of the largest thermal anomaly for the inferred source area (marked with a magenta cross in Figure 3) to estimate thermal fluxes of individual seafloor discharge sites in section 6.

4.2. Interval 2 (3000–3800 m)

[20] Hydrothermal anomalies in this "lower" depth interval are ubiquitous within the survey region (Figures 5a and 5b), and are often associated with corresponding *Eh* anomalies (Figures 5c and 5d). Because the *Eh* signal equilibrates more rapidly than the temperature signal, it is particularly useful for grouping anomalies into clusters associated with discrete seafloor discharge sites. Most of the *Eh* anomalies observed in this depth interval have corresponding thermal anomalies, but some do not, which implies that in some places the hydrothermal fluids have compositional, but not thermal, signals. This situation might occur, for example, by interaction of pore fluids with microbes, and we note that microbial mats covered large portions of the axial valley seafloor in our study area [*Helmke et al.*, 2007]. However, we restrict our analyses to those observations that contain thermal anomalies because they constitute the majority of our plume data, and because compositional anomalies are beyond the scope of our modeling effort.

[21] We constructed horizontal transects from our CTD data to help interpret the observations from the spatially disparate casts (Figures 6–8). Based on inspection of these transects and the map view data of Figure 5 we group the plume anomalies into seven spatially distinct sets. This grouping is subject to interpretation, and it is possible to envision as few as three discrete groups depending on the impact of temporal aliasing and out-of-plane effects in our transects, which were acquired over a 14 day period. There is clearly a "cloud" of hydrothermal plume fluids that overlies much of our survey region in this depth interval, but the *Eh* data, in particular, indicate that this cloud is generated by several different source regions. We discuss the anomaly patterns along three transects in Interval 2 and their implications for seafloor source regions below.

4.2.1. Oden Volcano to Duque's Hill Transect

[22] We find evidence for two or three discrete seafloor discharge sites on the transect shown in Figure 6 running from the SW side of Oden volcano [*Sohn et al.*, 2008] to Duque's Hill in the center of the axial valley. There appears to be a discharge site somewhere SW of Oden volcano (source 7 in Figure 1) that creates the anomaly pattern delineated with a black ellipse in Figures 6b and 6c. This set

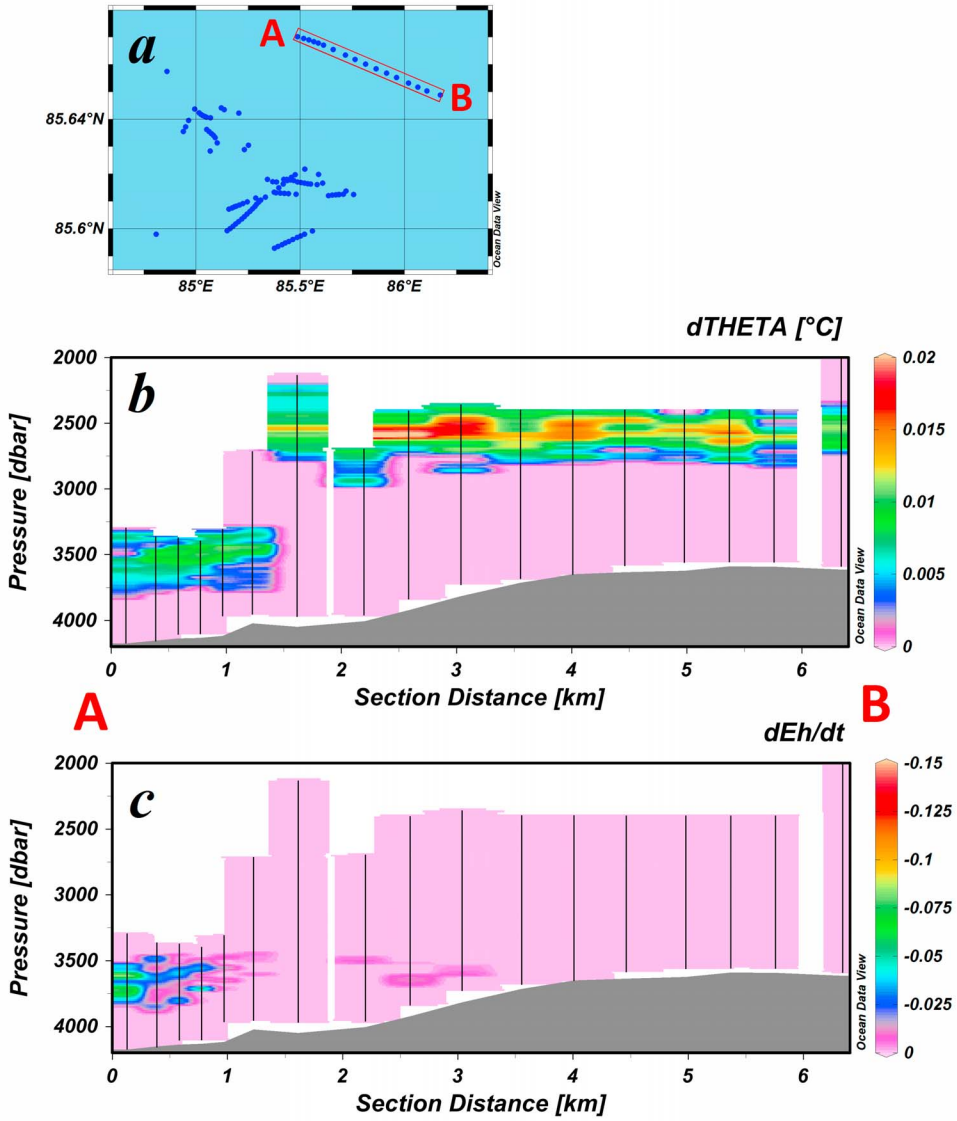

Figure 4. (a) Overview map with all CTD downcasts marked with blue circles where A and B indicate beginning and end of the transect, respectively. The transect with CTD downcasts as black vertical lines, from within the red box in Figure 4a, showing (b) $\delta\Theta$ and (c) *Eh* anomalies.

of anomalies is spatially distinct from those observed over Oden volcano and also NE toward Duque's Hill, and is therefore interpreted as originating from a distinct seafloor source. The other two sets of anomalies, which are delineated with red ellipses in Figures 6b and 6c, might originate from a single source, but the *Eh* data suggest two discrete sources (sources 6 and 4 in Figure 1). Camera tows over Oden volcano revealed abundant microbial mats within the central crater and also covering portions of the volcano's flanks [*Pontbriand et al.*, 2008], which implies that there is a subsurface source of hydrothermal fluids providing metabolic energy for cell growth in these microbes [*Helmke et al.*, 2007], supporting the interpretation of a discharge site somewhere within, or near, this volcanic edifice. The interpretation of an additional site on Duque's Hill (source 4 in Figure 1) is more equivocal, as the observed anomalies could also potentially be the result of time space aliasing from a more distant site (e.g., source 6).

4.2.2. Oden Volcano to Loke Volcano Transect

[23] We find evidence for one or two discrete seafloor discharge sites on the transect shown in Figure 7 running from Oden volcano to Loke volcano. The *Eh* anomalies near Loke volcano in Figure 7c that are marked with a red ellipse constitute a weak signal, but they reside at a slightly deeper depth interval than the *Eh* anomalies in near Oden volcano (sources 4, 6, and 7), and they are separated in the horizontal plane by ~3 km. We therefore interpret these anomalies as having been generated by a separate seafloor discharge site (Figure 1, source 8), and we note that Loke volcano contained some of the freshest (looking) lavas observed anywhere on the seafloor at 85°E during the AGAVE expedition, including ropey sheet flows [*Willis et al.*, 2007], and iron-oxidizing microbial mats [*Helmke et al.*, 2007].

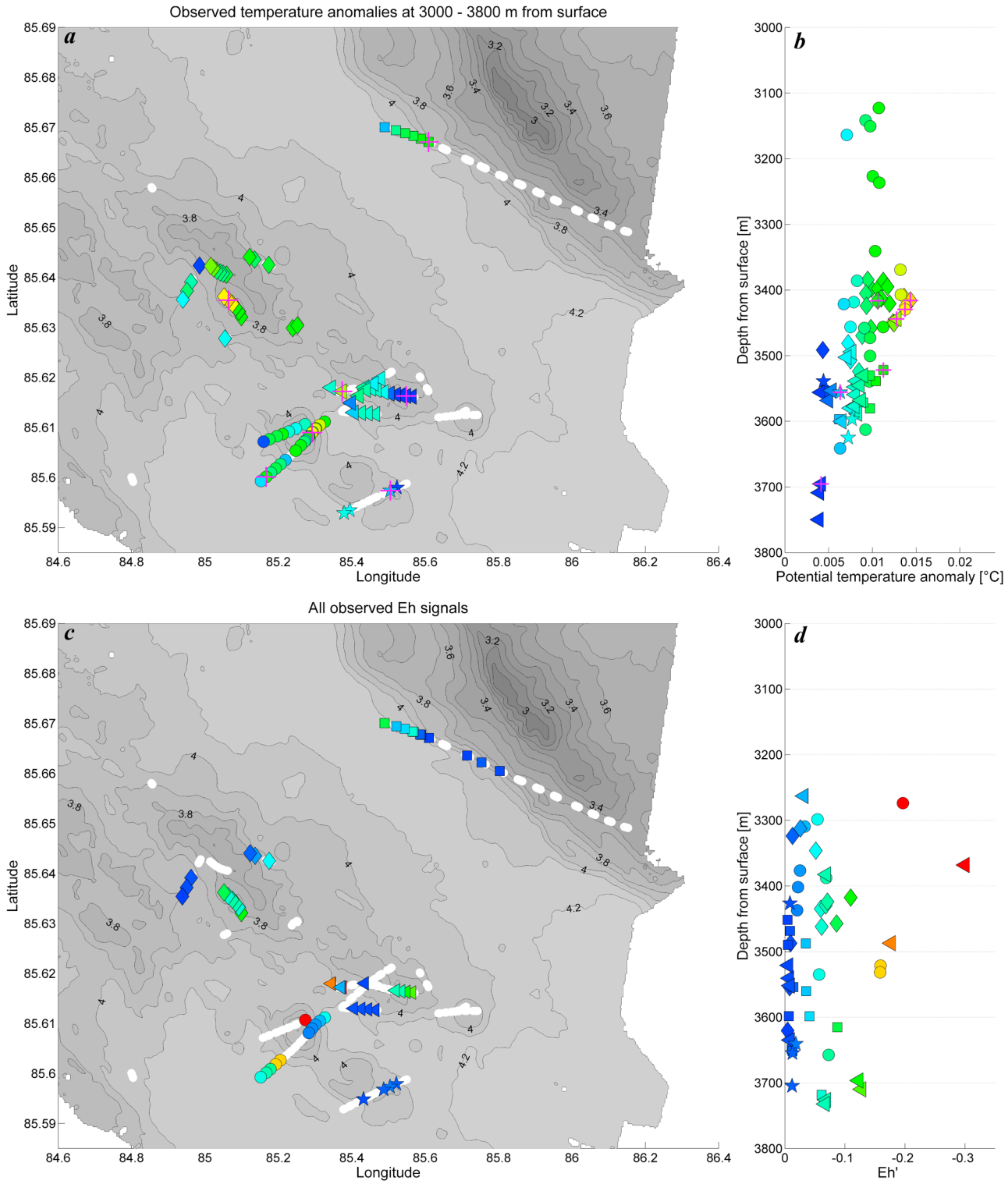

Figure 5. The (a and c) horizontal and (b and d) vertical distributions of the anomalies observed in depth Interval 2 (3000–3800 m). Thermal anomalies (Figures 5a and 5b) and Eh anomalies (Figures 5c and 5d). White circles indicate CTD profiles where no anomalies were detected. Magenta crosses indicate position of the maximum thermal anomaly observed for each discrete spatial set of combined thermal/Eh anomalies. The gray contours indicate bottom depth in km.

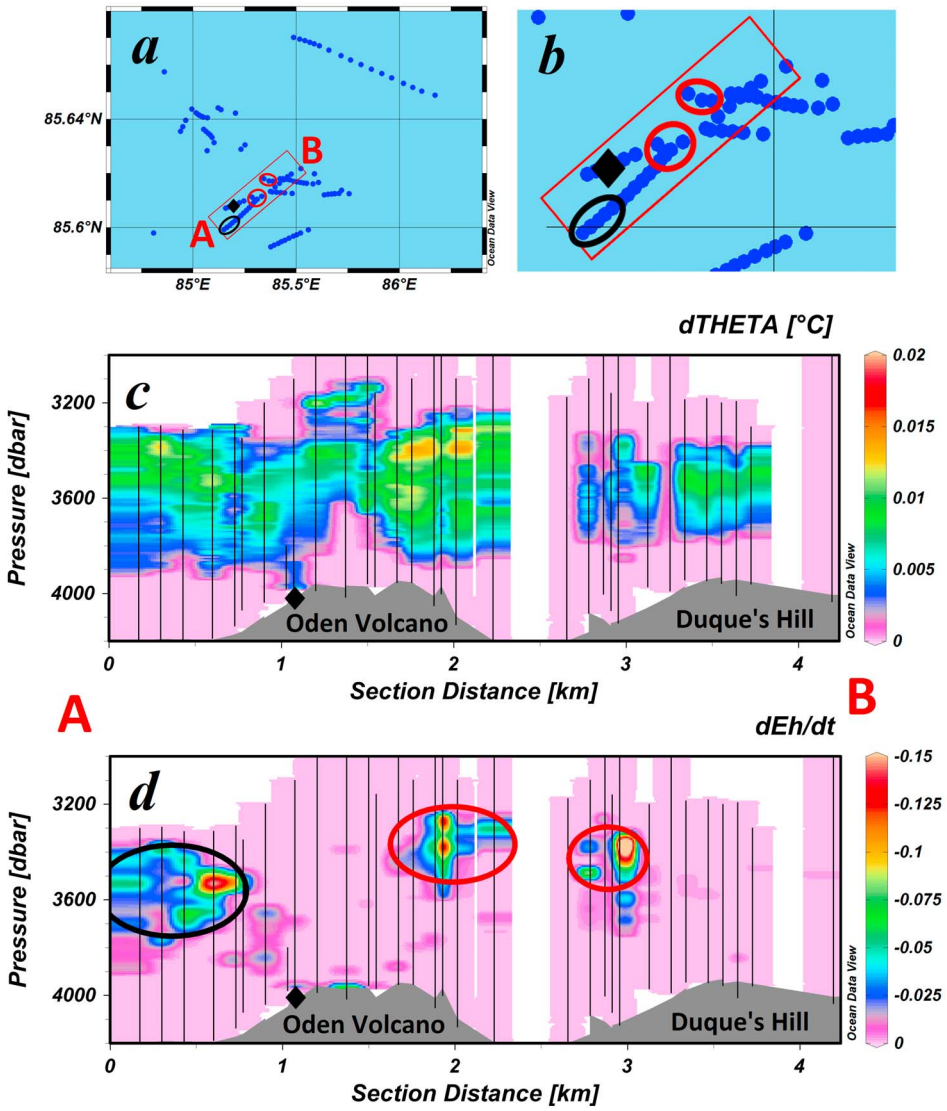

Figure 6. Oden Volcano to Duque's Hill transect. (a) Overview map with all CTD downcasts marked with blue circles where A and B indicate beginning and end of the transect, respectively. (b) Enlargement of the section A–B in Figure 6a. The transect with CTD downcasts as black vertical lines, from within the red box in Figures 6a and 6b, showing (c) $\delta\Theta$ and (d) *Eh* anomalies. The black and red ellipses in Figures 6a and 6b correspond to the black and red ellipses in Figure 6d. The location where we observed a buoyant plume (negative density gradient with depth) is marked with a black diamond.

We also note that black smoke was observed in the water column at an altitude of ~50 m above the seafloor in the immediate vicinity of this inferred source (but no vent fields were observed when the camera system landed on the seafloor several minutes later). The anomalies indicated by the black ellipse in Figure 7 constitute a relatively strong *Eh* signal, but without a corresponding temperature anomaly. As described earlier, although these anomalies may be indicative of a seafloor venting site, we do not attempt to constrain the nature of the source because our modeling is restricted to thermally buoyant plumes.

4.2.3. Jessica's Hill to Duque's Hill Transect

[24] We find evidence for one or two discrete seafloor discharge sites in a transect running between the two major constructional volcanic lineations in the center of the axial valley (Figure 8). There are three discrete *Eh* anomalies in this transect, but one of them (not circled in Figure 8c) is a projection of an anomaly that has already been interpreted in the Oden volcano to Duque's Hill transect. The other two *Eh* anomalies (red and black ellipses in Figure 8c) appear to represent discrete seafloor discharge sites (Figure 1, sources 3 and 5), although this interpretation could be erroneous if the *Eh* signals can persist within the Arctic Ocean water column longer than the ~3 days it would take plume fluids to traverse the distance from Duque's Hill to Jessica Hill. There appears to be an essentially continuous thermal anomaly connecting all of these sites, but the *Eh* data seem to indicate discrete seafloor sources.

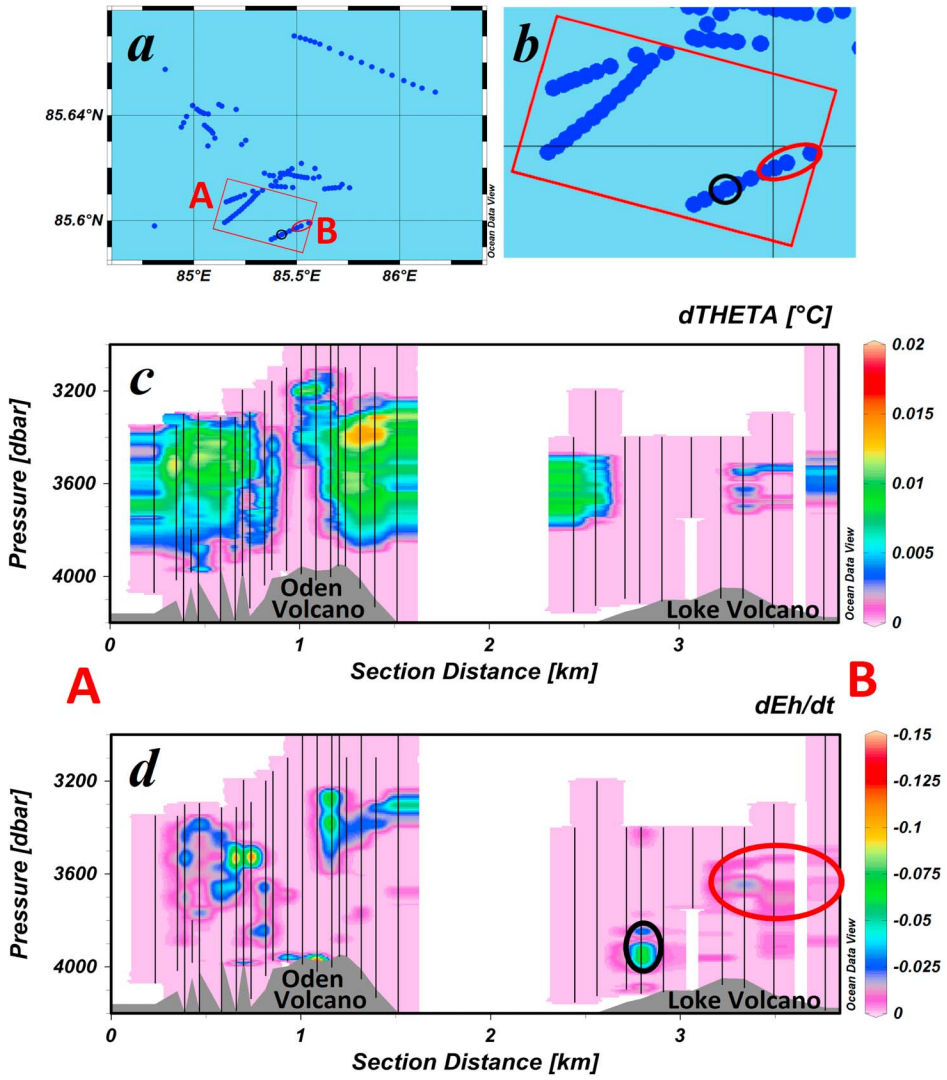

Figure 7. Oden volcano to Loke volcano transect. (a) Overview map with all CTD downcasts marked with blue circles where A and B indicate beginning and end of the transect, respectively. (b) Enlargement of the section A–B in Figure 7a. The transect with CTD downcasts as black vertical lines, from within the red box in Figures 7a and 7b, showing (c) $\delta\Theta$ and (d) *Eh* anomalies. The black and red ellipses in Figures 7a and 7b correspond to the black and red ellipses in Figure 7d.

4.2.4. Northern Axial Valley Wall Transect

[25] We find evidence for one seafloor discharge site contributing to plume anomalies observed in depth Interval 2 in a transect that runs obliquely to the northern axial valley wall (Figure 4). The *Eh* anomaly at the end of this transect is not vertically aligned with those from the central axial valley, and it is separated by > 5 km. We therefore interpret this signal as having been generated by a discrete seafloor source (Figure 1, source 2). No imagery of the seafloor is available from this region.

[26] In total, we find evidence for seven discrete seafloor discharge sites contributing plume fluids to depth Interval 2. But this interpretation is equivocal, and the number could be as low as three. As for Interval 1, we use the depth and magnitude of the largest thermal anomaly for each of the seven inferred source areas (marked with magenta crosses in Figures 5a and 5b) to estimate thermal fluxes of individual seafloor discharge sites in section 6.

5. Turbulent Plume Model

[27] We use a numerical model to constrain the heat flux of each discrete seafloor discharge site by comparison with our survey data. The model is based on the physics of *Morton et al.* [1956], but considers the heat content and salinity separately. The approach is similar to that of *Speer and Rona* [1989], except that rather than conserving temperature, we conserve heat. The state variables of the modeled plume are heat content *Q(z)*, salinity *S(z)*, vertical velocity *W(z)* and plume horizontal area *A(z)*. These variables represent the horizontally averaged properties of the flow (Figure 9).

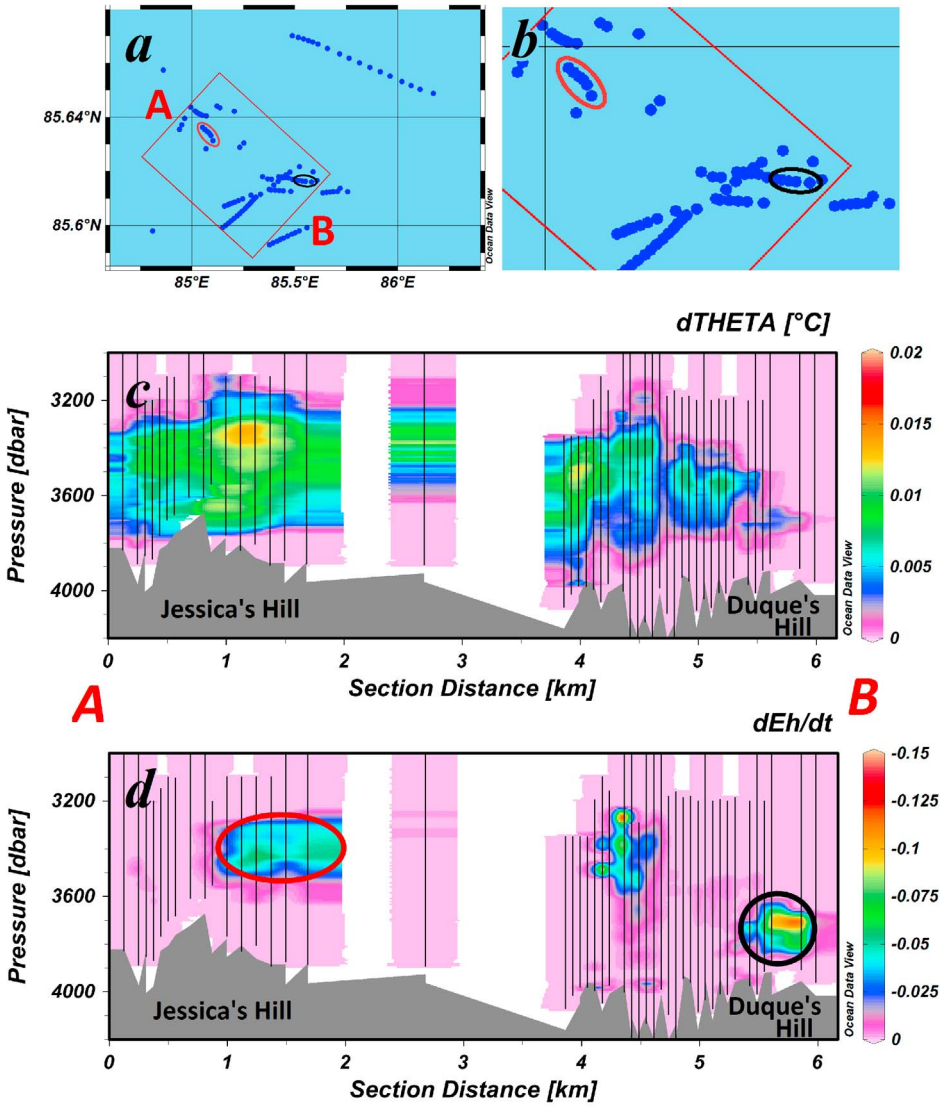

Figure 8. Jessica's Hill to Duque's Hill transect. (a) Overview map with all CTD downcasts marked with blue circles where A and B indicate beginning and end of the transect, respectively. (b) Enlargement of the section A–B in Figure 8a. The transect with CTD downcasts as black vertical lines, from within the red box in Figure 8a and 8b, showing (c) $\delta\Theta$ and (d) *Eh* anomalies respectively. The black and red ellipses in Figure 8a and 8b correspond to the black and red ellipses in Figure 8d.

[28] The basic assumption in this model is that the entrainment into the plume is proportional to the vertical velocity. The conservation equations for mass, heat, salinity and momentum are

$$(AW)_z = EA^{1/2}W, \tag{1}$$

$$(QAW)_z = \overline{Q}EA^{1/2}W, \tag{2}$$

$$(SAW)_z = \overline{S}EA^{1/2}W, \tag{3}$$

$$(AW^2)_z = g'A. \tag{4}$$

The subscript z is the vertical derivative, E is the entrainment coefficient (set to a constant value of 0.255, so that $\alpha_e = E/2\pi^{1/2} = 0.072$ according to *Speer and Rona* [1989]), and g' is the reduced gravity given by

$$g' = g\frac{\overline{\rho} - \rho}{\rho_0},$$

where g is the acceleration of gravity, $\bar{\rho}$ is the potential density of the background field, ρ is the plume potential density, and ρ_0 is the background potential density at the reference pressure of 3000 dbar. Temperature and heat content per unit volume are related by

$$Q = \rho C_p \Theta.$$

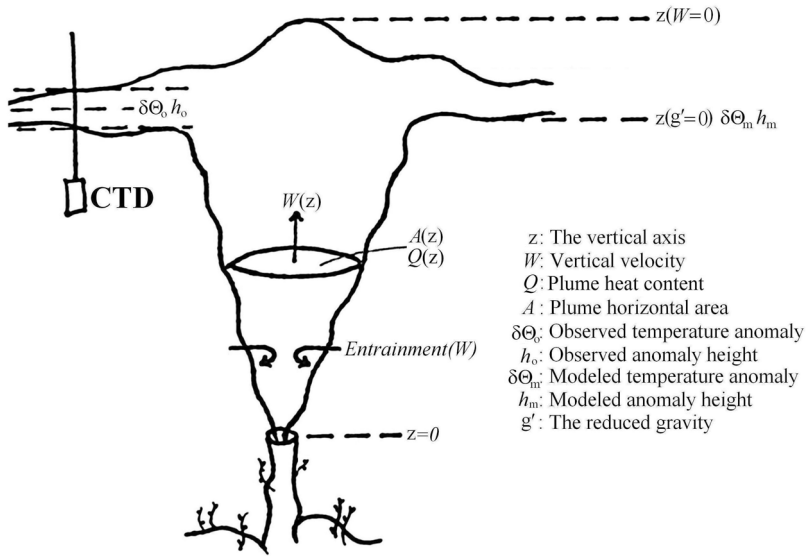

Figure 9. Schematic sketch over the modeled plume. Subscripts *m* and *o* stand for *model result* and *observations*, respectively.

Here C_p is the specific heat of salt water. Both C_p and ρ are calculated from the model presented by *Sun et al.* [2008] but for temperatures less than 23°C, the more accurate UNESCO 1983 equation of state is used for the density calculations [*Fofonoff and Millard*, 1983]. After rearranging equations (1)–(4), the ordinary differential equations are solved numerically in MATLAB using the ODE 45 solver [*Dormand and Prince*, 1980] and the potential temperature is calculated by iteration at each step.

[29] One difference between our approach and some earlier applications of this model is that we use an observed background profile instead of linear gradients of the background salinity and potential temperature. This distinction is important because the entire local water column is influenced by heat fluxes from multiple discharge sites that are mixed and advected, thereby creating nonlinear structures in the background temperature and salinity profiles.

[30] Ambient cross flows are not considered in this model. Earlier work [e.g., *Slawson and Csanady*, 1971; *Middleton*, 1986] showed that, for any given source, the rise height is reduced with increased cross flow velocity and increased stratification. For strong cross flows the buoyant part of the plume bends over, which also changes the entrainment assumption. Although we do not have data from any current meters at the 85°E segment, average speeds of 1 cm/s were measured by a freely drifting AUV hovering ~10 m above the axial valley floor over one complete semidiurnal tidal cycle. The results from a barotropic tide model show that over the period of the cruise the horizontal velocities due to the barotropic tide did not exceed 1.25 cm/s at the 85°E segment of the Gakkel Ridge. Because of the low current speeds and the extremely weak density stratification in the deep Arctic Ocean, ambient cross flow likely exerts a negligible effect on plumes in our study area.

[31] We ran the plume model with a range of possible initial condition combinations, and using thirteen different source depths between 3000 m and 4200 m (1.1 million model runs). The initial conditions were divided into two possible scenarios; a high-temperature, black-smoke-type *chimney discharge case* (CH), and a low-temperature *diffusive discharge case* (DD), see Table 1. We explicitly assume that black smoker discharge is accommodated by relatively small vents (chimney structures), whereas diffuse discharge may be accommodated over much larger areas [e.g., *Schultz et al.*, 1992]. The initial salinity was assumed to be equal to the salinity of the ambient water at the assumed vent depth [e.g., *Speer and Rona*, 1989] taken from the background salinity profile. This is an important assumption because the buoyancy of plume fluids is influenced by salinity, but we do not know the end-member exit fluid salinity for any of our inferred sources. For low temperature diffusive discharge sites the sensitivity of initial salinity is rather high due to the small initial density difference between the plume water and the ambient water. A small increase of the initial salinity can completely eradicate the initial buoyancy or even reverse it, which would then produce dense bottom currents rather than buoyant plumes. For high temperature sources the sensitivity is much smaller.

[32] We modeled source heat fluxes up to 40 GW, but the maximum value required to match our observations is ~10 GW, and so we only show results for initial fluxes less than this value. A comparison of the present numerical model to the *Speer and Rona* [1989] model and to an analytical expression based on scaling analysis [*Briggs*, 1969], is

Table 1. Initial Conditions Over Which the Model Was Run[a]

	$A(0)$ (m^2)	$\delta\Theta$ (0) (°C)	$W(0)$ (m/s)
CH	0.01–3.01	100–400	0.1–2.01
DD	10–10,000	0–10	0.001–0.101

[a]CH is meant to represent a plausible parameter range for black smoker chimneys, and DD is meant to represent a plausible parameter range for diffusive discharge.

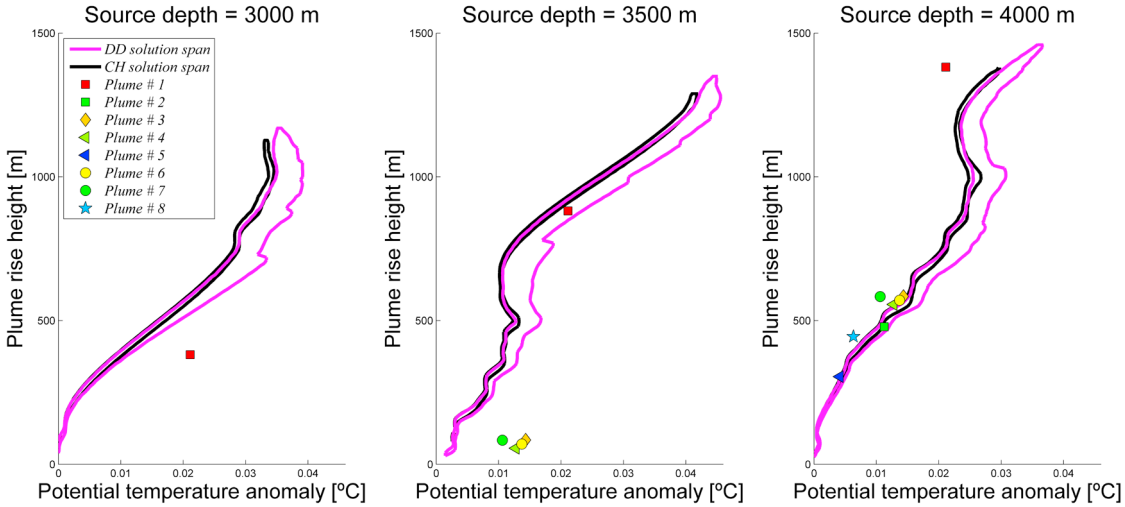

Figure 10. Model solution span $\delta\Theta_m$ plotted against h_m for the model runs over the chimney range (black) and over the diffusive discharge range (magenta). Also plotted are the 8 maximum thermal anomalies observed for each discrete plume source region (from Figures 3, 5a, and 5b and Table 4). These results show, for example, that the source depths of 3000 m and 3500 m are too shallow but 4000 m is plausible for the lower plumes 2–8. Note that the "shape" of the solution space varies as a function of source depth because of nonlinear potential temperature and salinity structure in our study area.

shown in the Appendix where also the sensitivity and choice of the entrainment parameter value is discussed.

6. Modeling Results and Fit to Observations

[33] We varied the initial conditions (depth, cross-sectional area, exit fluid temperature, and exit fluid velocity) in our plume model to cover the plausible range of venting conditions that could have produced the anomalies we observed at the 85°E segment of the Gakkel Ridge. For each spatially distinct set of observed anomalies we identified the position and amplitude of the maximum thermal anomaly, and we took this as our best proxy for the putative center of the neutrally buoyant plume layer for each source. We can then compare the model solution space to our observations in order to place some constraints on the thermal power (heat flux) and source depth of the individual plume sources.

[34] For each inferred source, we compare the maximum observed thermal anomaly to the range of model outputs (rise height and corresponding temperature anomaly). The rise height is defined as the depth where the buoyancy becomes zero, which corresponds roughly with the "lower edge" of the neutrally buoyant plume layer. The reason for this definition of rise height is because the temperature anomaly at this level is the upper limit for the whole neutrally buoyant plume. If a set of model parameters produces a neutral plume at the observed depth horizon with a thermal anomaly that is greater than or equal to the observed maximum anomaly, then we consider these to be a plausible set of parameters for the inferred vent field source (Figure 10). The heat flux ΔH is then calculated for all plausible parameter combinations according to

$$\Delta H = \rho(0) C_p(0) \delta\Theta(0) A(0) W(0). \quad (5)$$

The results of applying this procedure for the complete range of black smoker and diffuse flow model parameters are tabulated in Tables 2 and 3. For each inferred source we also identify the "best fitting" parameter combination, which is defined as the set of parameters that most closely matches the observed amplitude and depth of the maximum thermal anomaly. We note that it is necessary to formally vary depth as a source parameter because of the nonlinear background potential temperature and salinity gradients in our study area, as can be seen via inspection in Figure 10.

[35] The model outputs the depth and amplitude of the thermal anomaly close to the center of the neutrally buoyant plume, such that the accuracy of our estimates therefore depends on the proximity of our maximum thermal anomaly observation to the actual plume center. We systematically underestimate the maximum plume anomaly in proportion to the distance of our maximum thermal anomaly observation from the actual plume center. This may be the case for plume 7, where the nominal rise height (i.e., the rise height if assuming a source depth equal to the seafloor depth immediately below the observed plume) exceeds the best fit rise height by more than 300 m. According to Tables 2 and 3, if we use the nominal source depth (marked with footnotes), we would get a heat flux of about 200 MW as opposed to our best fit model values of 20 MW. Nevertheless, because the depth (i.e., rise height) and amplitude of the thermal anomalies in the neutrally buoyant plume are controlled to first order by the thermal power of the seafloor source, we can place useful (conservative) constraints on the size of the inferred plume sources by comparing the model solution space to our observations.

[36] We appear to have made one observation in a buoyant plume stem (as evidenced by a negative potential density gradient with depth). Because the lateral spreading of a plume is limited until it reaches the level of neutral buoyancy, the seafloor discharge site is located in close

Table 2. Best Fit Source Heat Flux for Diffusive Discharge Initial Condition Combinations[a]

Source Depth (m)	Plume 1	Plume 2	Plume 3	Plume 4	Plume 5	Plume 6	Plume 7	Plume 8
3000	-	-	-	-	-	-	-	-
3100	-	-	-	-	-	-	-	-
3200	-	-	-	-	-	-	-	-
3300	-	-	-	-	-	-	-	-
3400	1270	-	-	-	-	-	-	-
3500	**1850**	-	-	-	-	-	-	-
3600	1970	-	-	-	-	-	-	-
3700	2460	-	-	-	-	-	-	-
3800	3520	-	-[b]	60	-	-	**20**	10
3900	4950[b]	70	**100**	**60**	-[b]	**70**[b]	50	**10**
4000	6740	**80**[b]	120	150[b]	**10**	180	110	30[b]
4100	8890	110	210	170	20	190	210[b]	70
4200	-	200	450	350	50	390	450	160

[a]Heat flux given in MW for the eight inferred sources (see Figure 1). The over all best fit is shown in bold.
[b]Depth matching seafloor depth immediately below observed plume anomalies (nominal source depth).

proximity (<~100 m) to the buoyant plume stem. The depth of the source is 3980 m and is shown in Figure 6 as a black diamond. We note that it is possible that this single source could have conceivably generated all of the anomalies observed along the Oden volcano to Duque's Hill transect (Figure 6).

[37] The black smoker and diffusive discharge scenarios yield similar estimates for source heat flux and depth. Overall, the best fitting black smoker model runs yield heat flux estimates that are somewhat smaller than the best fitting diffusive discharge model runs, but the source depth estimates are essentially identical. We cannot formally distinguish between the black smoker and diffusive discharge scenarios for any of the plume signals based on our model results, but we can make inferences based on results from other hydrothermal fields and high-definition images of the local seafloor at 85°E acquired during the AGAVE expedition.

[38] The large heat flux (~2 GW) required to fit the plume observations made in depth Interval 1 is indicative of a large, high-temperature hydrothermal field. The only other presently known deep sea fields with a heat flux of this same magnitude are the Trans-Atlantic Geotraverse (TAG) and Rainbow fields on the Mid-Atlantic Ridge, which are both large fields discharging fluids at temperatures of ~360°C [e.g., *Douville et al.*, 2002; *Sohn*, 2007; *Wichers et al.*, 2005]. There is no bottom imagery available from the seafloor beneath plume 1, but we note that it appears to be located near the axial valley wall, where large offset normal faults intersect the seafloor. This is consistent with the geological setting of the TAG and Rainbow fields, both of which are located above large-offset normal fault zones [e.g., *Douville et al.*, 2002; *deMartin et al.*, 2007].

[39] Plumes 3–8, with heat flux estimates ranging from 5 to 110 MW, all appear to be sourced from within the region of constructional volcanic features on the floor of the axial valley. No evidence of high-temperature, black smoker venting was observed in seafloor imagery acquired from this region during the AGAVE expedition, but black smoke was observed in the water column at an altitude of 90 m above the bottom less than 100 m from the maximum temperature anomaly associated with plume 8. Portions of the axial valley seafloor in this area are covered with microbial mats composed largely of iron oxidizing bacteria [*Helmke et al.*, 2007], particularly inside and around the small, cratered, volcanic features that are ubiquitous on the valley floor. Although there was no visual evidence of active hydrothermal discharge from these sites (i.e., no black smoke nor

Table 3. Best Fit Source Heat Flux for Black Smoker Discharge Initial Condition Combinations[a]

Source Depth (m)	Plume 1	Plume 2	Plume 3	Plume 4	Plume 5	Plume 6	Plume 7	Plume 8
3000	-	-	-	-	-	-	-	-
3100	-	-	-	-	-	-	-	-
3200	-	-	-	-	-	-	-	-
3300	-	-	-	-	-	-	-	-
3400	-	-	-	-	-	-	-	-
3500	1320	-	-	-	-	-	-	-
3600	**1810**	-	-	-	-	-	-	-
3700	2060	-	-	-	-	-	-	-
3800	2990	-	-[b]	-	-	-	**20**	-
3900	4070[b]	-	-	50	-[b]	60[b]	40	**10**
4000	-	70[b]	**110**	**80**	**5**	**100**	70	20[b]
4100	-	**80**	180	120[b]	10	160	180[b]	60
4200	-	130	380	290	40	330	380	130

[a]Heat flux given in MW for the eight inferred sources (see Figure 1). The over all best fit is shown in bold.
[b]Depth matching seafloor depth immediately below observed plume anomalies (nominal source depth).

Table 4. Characteristics of the Maximum Thermal Anomalies Associated With Eight Discrete Plumes Identified in the Survey Data[a]

	Plume 1	Plume 2	Plume 3	Plume 4	Plume 5	Plume 6	Plume 7	Plume 8
Latitude (°N)	85.66156	85.6671	85.63546	85.61722	85.61632	85.60898	85.60014	85.5974
Longitude (°E)	85.77218	85.60949	85.06400	85.37402	85.54880	85.29184	85.16674	85.50532
$\delta\Theta_o$ (°C)	0.021	0.011	0.014	0.013	0.004	0.014	0.011	0.006
NBL depth (m)	2620	3520	3420	3440	3700	3430	3420	3560
Nominal source depth (m)	3850	3970	3750	4050	3860	3900	4130	4000
BF source depth DD (m)	3500	4000	3900	3900	4000	3900	3800	3900
BF source depth CH (m)	3600	4100	4000	4000	4000	4000	3800	3900
Nominal rise height (m)	1230	440	340	610	160	470	710	440
BF rise height DD (m)	880	480	480	460	300	470	380	340
BF rise height CH (m)	980	580	580	560	300	570	380	340
DD heat flux(MW)	1850	80	100	60	10	70	20	10
CH heat flux(MW)	1810	80	110	80	5	100	20	10
Symbol	Red square	Green square	Yellow diamond	Lime tilted triangle	Blue tilted triangle	Yellow circle	Green circle	Light blue star

[a]Maximum thermal anomalies are marked with magenta crosses in Figures 3, 5a, and 5b. $\delta\Theta_o$ is the observed temperature anomaly, NBL depth is the observed neutral buoyant layer depth, nominal source depth is the bottom depth under the observed plume signals, BF depth is the best fit source depth based on model results, nominal rise height is the rise height estimated based on the distance from the anomaly to the seafloor immediately underneath, BF rise height is the best fit rise height based on model results, and CH heat flux and DD heat flux are the best fit heat flux estimates for the chimney case and the diffusive discharge case, respectively.

shimmering water), some of the highest Eh anomalies were observed just above the mats, and it seems likely that the microbes are deriving metabolic energy by oxidizing low-temperature hydrothermal fluids. This evidence suggests that some of the plume anomalies observed in depth Interval 2 over this central portion of the axial valley were generated by low-temperature, diffusive discharge.

[40] To summarize, we find evidence for up to eight discrete zones of hydrothermal discharge on the seafloor at the 85°E segment. Two of these appear to be hosted on normal faults hosting extension on the northern axial valley wall, and six of these appear to be associated with constructional volcanic features on the axial valley floor. The discharge zones on the normal fault zone have heat fluxes on the order of 2 GW and 50 MW, respectively, and the larger of these is likely a large, high-temperature vent field of the same size as the TAG and Rainbow fields on the MAR. The discharge zones on the valley floor have heat fluxes on the order of a few tens of MW up to ~100 MW, and thus are relatively small fields. Water column observations of black smoke indicate that plume 8 might be a high-temperature field. We do not have direct evidence to constrain the nature of discharge at the rest of the valley floor sites, but we have indirect evidence that at least some of these fields are sites of diffuse discharge of low-temperature hydrothermal fluids. The total hydrothermal heat flux for the 85°E segment from our best fitting initial combinations is ~2 GW, about 85% of which is due to plume 1. The characteristics of the eight inferred plumes are summarized in Table 4.

7. Discussion

[41] Our results provide new information regarding the nature of hydrothermal activity on the Gakkel Ridge at 85°E, and some clues regarding its relationship to volcanic activity and crustal extension. There appears to be a large vent field located on the fault terrace forming the north side of the axial valley with a heat flux of ~2 GW, which dominates hydrothermal fluxes in this region. It appears to be among the largest known vent fields in the deep sea, similar to the TAG and Rainbow fields on the MAR. Both TAG and Rainbow are located above long-lived, well-developed, extensional fault zones, and neither of these fields appear to be directly associated with volcanic activity [e.g., *deMartin et al.*, 2007; *Douville et al.*, 2002]. It therefore seems likely that the discharge site associated with plume 1 is a large, chronic, hydrothermal field that exploits a well-developed, deeply penetrating, fault zone to extract high-temperature heat from basal portions of the lithosphere and/or upper mantle, as opposed to a more ephemeral vent associated with recent volcanic activity.

[42] The 1999 earthquake swarm at 85°E began with large magnitude normal faulting [*Mueller and Jokat*, 2000], and some of these earthquakes may well have occurred on the fault system hosting fluid flow for plumes 1 and 2 (hypocentral uncertainties are too large to associate the events with specific fault zones). It therefore seems possible, if not likely, that the hydrothermal discharge from these sites was perturbed by the 1999 earthquake swarm. Interestingly, the thermal anomalies we measured in depth Interval 1 in 2007 were significantly smaller (0.02 versus 0.07°C) than those observed in the same depth interval in 2001 [cf., *Baker et al.*, 2004; *Edmonds et al.*, 2003]. This implies a fairly dramatic temporal evolution (decay) of the plume 1 source over the 6 year interval between the two surveys. However, this evolution cannot be explained solely by a decrease in hydrothermal flux. Because of the weak salinity gradient in the deep Arctic Ocean an enormous volume of ambient water needs to be mixed into the plume in order to produce a neutrally buoyant plume layer with a thermal anomaly of 0.07°C. Our model is unable to reproduce such an anomaly at 2500 m depth. A thermal output of 50 GW at 4000 m depth, for example, would produce an anomaly of about 0.06°C, but with a rise height of 2000 m (as opposed to 1500 m).

[43] At this point we can only speculate about the processes that generated the large thermal anomaly observed in Interval 1 during AMORE in 2001. One possibility would be that the 1999–2001 eruption generated an event plume associated with the catastrophic discharge of briney fluids that had accumulated within the crust as a result of phase separation [e.g., *Cann and Strens*, 1989]. Event plumes may

have large instantaneous thermal energies of the order several tens of GW, and if the fluids are brines, such as might have been generated by supercritical phase separation [e.g., *Foustoukos and Seyfried*, 2007], then they could probably generate a neutral plume layer with a thermal anomaly of 0.07°C at a depth of ~2500 m. Another possibility is that the plume observed in 2001 was formed at least partly as a result of the explosive discharge of magmatic jets into the water column. Volcaniclastic material attributed to this process blankets the axial valley at 85°E, and a potentially large fraction of the magma erupted during the volcanic event that began in 1999 was explosively discharged [*Sohn et al.*, 2008]. Evidence for Strombolian style explosive discharge was also detected by an ice-mounted seismometer network at the 85°E site in 2001 [*Schlindwein et al.*, 2007], suggesting that explosive activity was ongoing from 1999 until at least 2001. The physics and chemistry of magmatic jets discharging into the deep ocean is not well understood, but it has been hypothesized that these events can generate "megaplumes" [e.g., *Clague et al.*, 2009]. In either case our model results suggest that the plume observed in depth Interval 1 during AMORE in 2001 was not a chronic plume.

[44] These results also have implications for the hypothesis of *Baker et al.* [2004] that plume fluids from the 85°E segment were detected above the ridge axis more than 175 km away during AMORE in 2001. Plume fluids in depth Interval 1 are at a horizon above the walls of the axial valley, which means they lie above the topographic channel created by the Gakkel Ridge. Along-axis currents with an average value of 1 cm/s were measured in the axial valley at 85°E over one semidiurnal tidal cycle by a freely drifting AUV during the AGAVE expedition. It is possible that these currents extend into the water column above the axial valley, and if so, then perhaps the plume fluids could be channeled along the ridge axis. At a velocity of 1 cm/s the plume would traverse the 175 km distance to the 70°E segment in ~200 days. Plume fluids in depth Interval 2 are at a horizon below the walls of the axial valley, and thus are more likely to be trapped and channeled along the ridge axis, but our models indicate that the source fluxes are relatively small (<100 MW), which argues against detection at great distances.

Appendix A: Model Comparison

[45] In this section we provide a comparison of our numerical model with the analytical model of *Briggs* [1969] and the model of *Speer and Rona* [1989]. *Briggs* [1969] presented an expression based on scaling analysis for the plume maximum rise height, z_{max} as a function of the background stratification and initial buoyancy flux

$$z_{\max} = 3.8B^{1/4}N^{-3/4},$$

where the coefficient implicitly corresponds to $\alpha_e = 0.125$, B is the buoyancy flux at the source and N is the Brunt-Väisälä frequency given by

$$B = g'(0)W(0)A(0),$$

$$N = \sqrt{\frac{g}{\rho_0}\frac{\partial \overline{\rho}}{\partial z}},$$

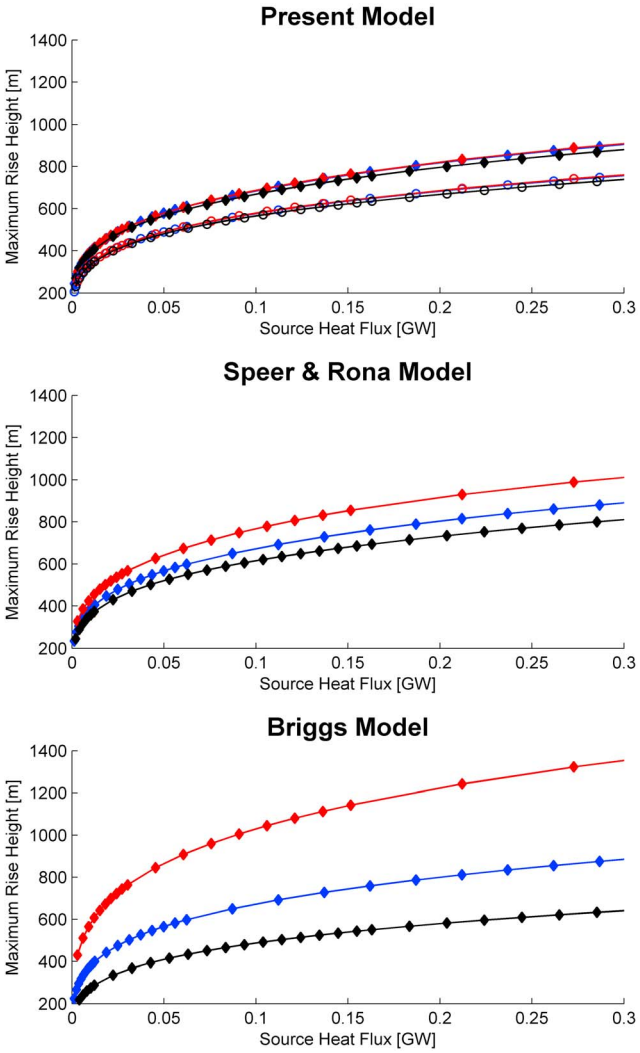

Figure A1. Maximum plume rise height plotted against source heat flux for the (top) present model, (middle) Speer and Rona model, and (bottom) Briggs model for $\delta\Theta$ (0) held constant at 5°C (black), 100°C (blue), and 400°C (red). Note that the blue and red curves are essentially identical in Figure A1 (top), such that the blue curves are difficult to discern beneath the red curves. We also show results from our numerical model using a different entrainment coefficient (i.e., $\alpha_e = 0.09$, 25% increase) as circle symbols (as opposed to diamonds) in Figure A1 (top).

respectively. N is constant here and based on linear regression of the observed background potential density profile. The Speer and Rona model is similar to ours except that we use nonlinear temperature, pressure and salinity dependent functions for C_p and ρ in our model, and we use heat instead of temperature as one of the state variables.

[46] Our numerical model is compared to the scaling expression and with the numerical model by *Speer and Rona* [1989] in Figure A1, where the resulting z_{max} for different initial temperature anomalies are plotted against the source heat flux given by equation (5).

[47] Comparing first Briggs' scaling expression with the numerical ones it is clear that the scaling expression has the highest sensitivity to the source potential temperature

anomaly. For the same heat flux the rise height is increased by more than a factor of two when increasing the source temperature anomaly from 5 to 400°C. The Speer and Rona model is less sensitive to changes in the source temperature anomaly while the present model is more or less invariant to the choice of source temperature, Figure A1. This implies that the rise height seems to be a function of heat flux only, when heat is fully conserved as in our model. The error in maximum rise height for the scaling expression is about 50% according to *Carazzo et al.* [2008] and we suggest that the lack of heat conservation might explain part of the error, although further studies are required in order to draw definite conclusions.

[48] It is evident that for an increase of the entrainment coefficient by 25% from (0.072 to 0.09) the maximum rise height is decreased by only 10%, Figure A1 (top). However, due to the small $dz_{max}/d\Delta H$ gradient, a small difference in rise height results in a significant change in heat flux estimate, especially at large rise heights. A constant entrainment coefficient has been employed in many other studies [e.g., *McDougall*, 1990; *Rudnicki and Elderfield*, 1992; *Speer and Rona*, 1989]. *Carazzo et al.* [2008], however, showed that a more sophisticated buoyancy dependent entrainment parameterization yields more accurate model results. Unfortunately, the implementation of a variable entrainment reduced our model run speed to such an extent that the large number of model runs carried out here would have been impractical. By choosing the rather low value of α_e we get about equal or smaller heat flux estimates compared to the variable entrainment for all types of initial conditions.

[49] **Acknowledgments.** We are grateful to the Swedish Polar Research Secretariat for the logistic support during the AGAVE expedition. We thank the crew of I/B *Oden* for their professionalism and support at sea during the expedition. We thank Marshall Swartz, Dan Torres, and George Tupper for CTD technical support and H. Edmonds, P. Winsor, and L. Upchurch for management and support of CTD operations at sea. The authors thank G. Björk and two anonymous reviewers for insightful comments on the manuscript and G. Carazzo for help with the implementation of variable entrainment into the plume model. K. Nakamura thanks Yoshifumi Nogi and the National Institute of Polar Research for travel and logistical support. This work was funded by the NSF Office of Polar Programs, Tellus—The Centre of Earth Systems Science at the University of Gothenburg, and the Woods Hole Oceanographic Institution.

References

Baker, E. T., Y. J. Chen, and J. P. Morgan (1996), The relationship between near-axis hydrothermal cooling and the spreading rate of mid-ocean ridges, *Earth Planet. Sci. Lett.*, *142*, 137–145, doi:10.1016/0012-821X(96)00097-0.

Baker, E. T., H. N. Edmonds, P. J. Michael, W. Bach, H. J. B. Dick, J. E. Snow, S. L. Walker, N. R. Banerjee, and C. H. Langmuir (2004), Hydrothermal venting in magma deserts: The ultraslow-spreading Gakkel and Southwest Indian Ridges, *Geochem. Geophys. Geosyst.*, *5*, Q08002, doi:10.1029/2004GC000712.

Björk, G., and P. Winsor (2006), The deep waters of the Eurasian Basin, Arctic Ocean: Geothermal heat flow, mixing and renewal, *Deep Sea Res. Part I*, *53*, 1253–1271, doi:10.1016/j.dsr.2006.05.006.

Briggs, G. A. (1969), Optimum formulas for buoyant plume rise, *Philos. Trans. R. Soc. London A*, *265*, 197–203, doi:10.1098/rsta.1969.0048.

Cann, J. R., and M. R. Strens (1989), Modeling periodic megaplume emission by black smoker systems, *J. Geophys. Res.*, *94*(B9), 12,227–12,237, doi:10.1029/JB094iB09p12227.

Carazzo, G., E. Kaminski, and S. Tait (2008), On the rise of turbulent plumes: Quantitative effects of variable entrainment for submarine hydrothermal vents, terrestrial and extra terrestrial explosive volcanism, *J. Geophys. Res.*, *113*, B09201, doi:10.1029/2007JB005458.

Clague, D. A., J. B. Paduan, and A. S. Davis (2009), Widespread strombolian eruptions of mid-ocean ridge basalt, *J. Volcanol. Geotherm. Res.*, *180*, 171–188, doi:10.1016/j.jvolgeores.2008.08.007.

deMartin, B., R. A. Sohn, J. P. Canales, and S. E. Humphris (2007), Kinematics and geometry of active detachment faulting beneath the Trans-Atlantic Geotraverse (TAG) hydrothermal field on the Mid-Atlantic Ridge, *Geology*, *35*(8), 711–714, doi:10.1130/G23718A.1.

Dick, H. J. B., J. Lin, and H. Schouten (2003), An ultraslow-spreading class of ocean ridge, *Nature*, *426*, 405–412, doi:10.1038/nature02128.

Dormand, J. R., and P. J. Prince (1980), A family of embedded Runge-Kutta formulae, *J. Comput. Appl. Math.*, *6*, 19–26, doi:10.1016/0771-050X(80)90013-3.

Douville, E., J. L. Charlou, E. H. Oelkers, P. Bienvenu, C. F. Jove Colon, J. P. Donval, Y. Fouquet, D. Prieur, and P. Appriou (2002), The rainbow vent fluids (36°14′N, MAR): The influence of ultramafic rocks and phase separation on trace metal content in Mid-Atlantic Ridge hydrothermal fluids, *Chem. Geol.*, *184*, 37–48, doi:10.1016/S0009-2541(01)00351-5.

Edmonds, H. N., P. J. Michael, E. T. Baker, D. P. Connelly, J. E. Snow, C. H. Langmuir, H. J. B. Dick, R. Mühe, C. R. German, and D. W. Graham (2003), Discovery of abundant hydrothermal venting on the ultra-slow spreading Gakkel Ridge in the Arctic Ocean, *Nature*, *421*, 252–256, doi:10.1038/nature01351.

Edwards, M. H., G. J. Kurras, M. Tolstoy, D. R. Bohnenstiehl, B. J. Coakley, and J. R. Cochran (2001), Evidence of recent volcanic activity on the ultra-slow-spreading Gakkel Ridge, *Nature*, *409*(6822), 808–812, doi:10.1038/35057258.

Fofonoff, N. P., and R. C. Millard (1983), *Algorithms for Computation of Fundamental Properties of Seawater*, 53 pp., U. N. Educ. Sci. and Cult. Organ., Paris.

Foustoukos, D. I., and W. E. Seyfried (2007), Fluid phase separation process in submarine hydrothermal systems, *Rev. Mineral. Geochem.*, *65*(1), 213–239, doi:10.2138/rmg.2007.65.7.

German, C. R., and J. Lin (2004), The thermal structure of the oceanic crust, ridge-spreading and hydrothermal circulation: How well do we understand their inter-connections?, in *Mid-Ocean Ridges: Hydrothermal Interactions Between the Lithosphere and Oceans*, *Geophys. Monogr. Ser.*, vol. 148, edited by C R. German, J. Lin, and L. M. Parson, pp.1–18, AGU, Washington, D. C.

Helmke, E., et al. (2007), Microbial communities at non-volcanic and volcanic sites of the Gakkel Ridge, *Eos Trans. AGU*, *88*(52), Fall Meet. Suppl., Abstract OS42A-01.

Jones, E. P., B. Rudels, and L. G. Andersson (1995), Deep waters of the Arctic Ocean: Origins and circulation, *Deep Sea Res. Part I*, *42*, 737–760, doi:10.1016/0967-0637(95)00013-V.

McDougall, T. J. (1990), Bulk properties of "hot smoker" plumes, *Earth Planet. Sci. Lett.*, *99*(1–2), 185–194, doi:10.1016/0012-821X(90)90081-8.

Michael, P. J., et al. (2003), Magmatism and amagmatic seafloor generation at the ultraslow-spreading Gakkel Ridge, Arctic Ocean, *Nature*, *423*, 956–961, doi:10.1038/nature01704.

Middleton, J. H. (1986), The rise of forced plumes in a stably stratified crossflow, *Boundary Layer Meteorol.*, *36*, 187–199, doi:10.1007/BF00117467.

Morton, B. R., G. I. Taylor, and J. S. Turner (1956), Turbulent gravitational convection from maintained and instantaneous source, *Proc. R. Soc. London A*, *234*, 1–23, doi:10.1098/rspa.1956.0011.

Mueller, C., and W. Jokat (2000), Seismic Evidence for volcanic activity discovered in central Arctic, *Eos Trans. AGU*, *81*(24), 265, 269.

Nøst, O. A., and P. E. Isachsen (2003), The large scale time-mean ocean circulation in the Nordic seas and the Arctic Ocean estimated from simplified dynamics, *J. Mar. Res.*, *61*, 175210, doi:10.1357/002224003322005069.

Padman, L., and S. Erofeeva (2004), A barotropic inverse tidal model for the Arctic Ocean, *Geophys. Res. Lett.*, *31*, L02303, doi:10.1029/2003GL019003.

Pontbriand, C. W., S. A. Soule, R. A. Sohn, and S. E. Humphris (2008), Deep pyroclastic deposits and evidence for explosive volcanism on the ultraslow spreading Gakkel Ridge at 85E, *Eos Trans. AGU*, *89*(53), Fall Meet. Suppl., Abstract T43B-2019.

Rudnicki, M. D., and H. Elderfield (1992), Theory applied to the Mid-Atlantic Ridge hydrothermal plumes—The finite-difference approach, *J. Volcanol. Geotherm. Res.*, *50*(1–2), 161–172, doi:10.1016/0377-0273(92)90043-D.

Schlindwein, V., C. Müller, and W. Jokat (2007), Microseismicity of the ultraslow-spreading Gakkel Ridge, Arctic Ocean: A pilot study, *Geophys. J. Int.*, *169*, 100–112, doi:10.1111/j.1365-246X.2006.03308.x.

Schlosser, P., B. Kromer, B. Ekwurzel, G. Bonisch, and J. H. McNichol (1997), The first trans-arctic 14C section: Comparison of the mean ages of the deep waters in the Eurasian and Canadian basins of the Arctic Ocean, *Nucl. Instrum. Methods Phys. Res. Sect. B*, *123*, 431–437.

Schultz, A., J. R. Delaney, and R. E. McDuff (1992), On the partitioning of heat flux between diffuse and point source seafloor venting, *J. Geophys. Res.*, *97*, 12,299–12,314, doi:10.1029/92JB00889.

Sella, G. F., T. H. Dixon, and A. Mao (2002), REVEL: A model for recent plate velocities from space geodesy, *J. Geophys. Res.*, *107*(B4), 2081, doi:10.1029/2000JB000033.

Slawson, P. R., and G. T. Csanady (1971), The effect of atmospheric conditions on plume rise, *J. Fluid Mech.*, *47*, 33–49, doi:10.1017/S0022112071000910.

Sohn, R. A. (2007), Stochastic analysis of exit fluid temperature records from the active TAG hydrothermal mound (Mid-Atlantic Ridge, 26°N): 1. Modes of variability and implications for subsurface flow, *J. Geophys. Res.*, *112*, B07101, doi:10.1029/2006JB004435.

Sohn, R. A., et al. (2008), Explosive volcanism on the ultraslow-spreading Gakkel Ridge, Arctic Ocean, *Nature*, *453*, 1236–1238, doi:10.1038/nature07075.

Speer, K. G., and P. A. Rona (1989), A model of an Atlantic and Pacific hydrothermal plume, *J. Geophys. Res.*, *94*(C5), 6213–6220, doi:10.1029/JC094iC05p06213.

Sun, H. B., et al. (2008), New equations for density, entropy, heat capacity, and potential temperature of a saline thermal fluid, *Deep Sea Res. Part I*, *55*(10), 1304–1310, doi:10.1016/j.dsr.2008.05.011.

Thorpe, S. A. (2005), *The Turbulent Ocean*, vol. xviii, 439 pp., Cambridge Univ. Press, Cambridge, U. K.

Tolstoy, M., D. R. Bohnenstiehl, M. H. Edwards, and G. J. Kurras (2001), Seismic character of volcanic activity at the ultraslow-spreading Gakkel Ridge, *Geology*, *29*(12), 1139–1142, doi:10.1130/0091-7613(2001)029<1139:SCOVAA>2.0.CO;2.

Turner, J. S. (1973), *Buoyancy Effects in Fluids*, vol. xv, 367 pp., Cambridge Univ. Press, Cambridge, U. K.

Turner, J. S. (1986), Turbulent entrainment-The development of the entrainment assumption, and its application to geophysical flows, *J. Fluid Mech.*, *173*, 431–471, doi:10.1017/S0022112086001222.

Upchurch, L., H. N. Edmonds, J. Resing, K. Nakamura, N. Buck, B. Liljebladh, C. Stranne, G. Tupper, and P. Winsor (2007), Geochemical characterization of hydrothermal plume fluids from peridotite- and basalt-dominated regions of the ultra-slow spreading Gakkel Ridge, *Eos Trans. AGU*, *88*(52), Fall Meet. Suppl., Abstract OS43A-0993.

Wichers, S., R. Reves-Sohn, and G. Terray (2005), New constraints on the thermal power of the TAG hydrothermal system and the dynamics of the water column plume, *Eos Trans. AGU*, *86*(52), Fall Meet. Suppl., Abstract OS33A-1466.

Willis, C., S. Humphris, S. A. Soule, R. Reves-Sohn, T. Shank, and H. Singh (2007), Volcanic structure of the Gakkel Ridge at 85°E, *Eos Trans. AGU*, *88*(52), Fall Meet. Suppl., Abstract OS43A-0986.

B. Liljebladh and C. Stranne, Department of Earth Sciences, University of Gothenburg, Box 460, SE-413 20, Gothenburg, Sweden. (beli@gvc.gu.se; christian.stranne@gvc.gu.se)

K. Nakamura, National Institute of Advanced Industrial Science and Technology, AIST Tsukuba Central 7, 1-1-1 Higashi, Tsukuba, Ibaraki 305-8567, Japan. (koichi.nakamura@aist.go.jp)

R. A. Sohn, Woods Hole Oceanographic Institution, 360 Woods Hole Rd., Mail Stop 24, Woods Hole, MA 02543, USA. (rsohn@whoi.edu)